ARTICLE TEMPLATE

Anomalous diffusion, dilation, and erosion in image processing

Andreas Kleefeld[a], Sophia Vorderwülbecke[a], and Bernhard Burgeth[b]

[a]Forschungszentrum Jülich GmbH, Jülich Supercomputing Centre, Jülich, Germany; [b]Saarland University, Department of Mathematics and Computer Science, Saarbrücken, Germany

ARTICLE HISTORY
Compiled September 21, 2017

ABSTRACT
In this paper, anomalous sub- and super-diffusion arising in image processing is considered and is modelled by a diffusion equation with fractional time derivative. It might serve as a building block for the construction of various filters. The resulting partial differential equation is discretised in space with centred differences and in time with the explicit or implicit Euler method, respectively. A numerical investigation is performed to illustrate new and interesting results. Additionally, the time derivative of the partial differential equation describing dilation and erosion is replaced by a fractional time derivative and then solved numerically. Interesting new questions arise from the presented numerical results. A short summary and outlook conclude this article.

KEYWORDS
anomalous diffusion; fractional derivative; Caputo; image processing; dilation; erosion; co-histogram

AMS CLASSIFICATION
34A08; 35R11; 68U10

1. Introduction

A large amount of methods for the processing and analysis of digital images employ time-dependent partial differential equations. It started out with the so-called scale-space concept introduced as early as 1959 by the works of T. Iijima [23, 24], although his efforts remained unrecognised for decades in the western image processing community. There, Witkin [48] had been considered for a long time to be the first to take advantage of the convolution of an image $f : \mathbb{R}^2 \longrightarrow \mathbb{R}$ with a Gaussian kernel establishing a semigroup structure. This approach is equivalent to solving the basic linear diffusion equation with Laplace operator Δ, i.e.

$$\frac{\partial u}{\partial t} = \Delta u \tag{1}$$

with initial condition $u(x, y, 0) = f(x, y)$ and homogeneous Neumann boundary conditions as Koenderink pointed out in [28]. The path-breaking work of Perona and

CONTACT Andreas Kleefeld. Email: a.kleefeld@fz-juelich.de

Malik [35] presenting a non-linear diffusion equation, where the diffusive properties of the equation are guided by the underlying image structure, mark the onset of image processing with highly non-linear evolution equations (see also Weickert [46]). Aside from these parabolic type equations derived from (1), other examples are transport equations such as

$$\frac{\partial u}{\partial t} = \|\nabla u\| \quad \text{and} \quad \frac{\partial u}{\partial t} = -\|\nabla u\| \tag{2}$$

with initial condition $u(x, y, 0) = f(x, y)$ and homogeneous Neumann boundary conditions, where $\|\cdot\|$ stands for a vector norm in $\mathbb{R}^2$. They mimic the process of dilation and erosion of an image [6, 43, 44] known from mathematical morphology [31, 39] and serve as building blocks for more higher morphological operations such as opening, closing, gradients (internal, external, and Beucher), and morphological Laplacian. In practice, the equations are solved approximately by specialized and elaborate numerical methods to obtain a processed image u.

In this article, a different type of generalization of an evolution equation is proposed. In the aforementioned equations a temporal derivative of fractional order α: $\partial^\alpha/\partial t^\alpha$ with $\alpha \in (0, 2)$ instead of a temporal derivative (of order one) $\partial/\partial t$ is considered. The question of a fractional differentiation has been raised by Leibniz (see for example [36]) making the idea almost as old as differential calculus itself. Hence, it is not a surprise that there are many legitimate ways to define a fractional derivative. Here, we will concentrate on a prominent approach named after Caputo [10] relying on fractional integration, a rather straightforward extension of integration, which is then concatenated with a regular differentiation. Clearly, differentiation is a local operation, while integration (fractional or not) acts globally. Therefore, fractional (Caputo-) differentiation takes global information into account. This made the approach attractive for researchers in various fields, such as classical mechanics, field theory, quantum mechanics, see, for example [1, 2, 21, 32], and the literature cited therein. Even in image processing the concept of fractional derivatives has been exploited, refer to [12], [49], and [11, 25, 50]. However, in most applications both temporal and spatial derivatives have been "fractioned", and very often the investigation concentrates on a specific fraction $\alpha = 1/2$, see [32] or [9]. In this article, we investigate the solutions of the morphological equations (2) (and for the sake of completeness the diffusion equation (1)), where the temporal derivative is replaced by a (Caputo-)fractional one with order α.

The motivation behind the use of a fractional time derivative especially of Caputo-type lies in its non-local structure in time. The integral appearing in its definition is a global operator in that the whole time history of the function is involved for the computation of the time fractional derivative. This interpolation between derivatives makes the computation more expensive. We use the Caputo time derivative as the right hand side in an evolution equation that governs the processing of an image which is used as initial data.

Again, we would like to emphasise that linear diffusion arises in many different disciplines such as (a) filling holes in complex surfaces using volumetric diffusion [13], (b) diffusion-based method for producing density-equalizing maps [18] as well as in (c) image processing (Perona-Malik diffusion and variants), see [46] and the references therein. The main assumption in image processing is the linearity of the diffusion process. Hence, its solution is given by means of a so-called semi-group of kernel functions. This is expressed by saying that the diffusion process has a scale-space property

or constitutes a scale space. It is worth noting that fractional integration constitutes a scale-space. Surprisingly, this is not true for fractional differentiation, although its definition is based on fractional integration. This complicates the numerical treatment but raises the expectations of the experimental results especially if we consider, as a novelty, the time fractional non-linear eikonal equations describing the dilation and erosion process of mathematical morphology. From a theoretical point of view, these eikonal equations do have a semigroup-property as well, since the classical set theoretic counterparts of dilation and erosion with respect to a fixed structuring element form a semigroup (see [41]). For example a dilation with time $2 \times T$ of a black image with a circular white structure in its center would lead to an extension of this structure twice as big as for the evolution time T. However, since we have to rely on numerical schemes this effect is overlaid by numerical dissipation causing blurring artifacts in the final results. With our approach we are capable to produce images with either sub-diffusion or super-diffusion which then might serve as initial images in test examples for algorithms designed for image deblurring, the "inverse" operation to blurring caused by diffusion processes. A well-known example is the Wiener filter which aims at the reversal of the blurring of an image induced by classical linear diffusion (see [45] for a good overview of some recent methods).

The structure of the paper is the following. In Sec. 2, the equation describing anomalous sub-diffusion is presented. Additionally, it is shown in detail how to solve this equation numerically. Next, the process of modified dilation and erosion is described in Sec. 3 as well as the discretisation. In Sec. 4, numerical results are reported. A short summary and outlook conclude this article.

2. Anomalous sub-diffusion and super-diffusion

Anomalous diffusion is modelled by the partial differential equation

$$\frac{{}^{C}\partial^{\alpha} u}{\partial t^{\alpha}} = \operatorname{div}(\kappa \operatorname{grad} u)\,. \tag{3}$$

Here, κ denotes either a constant or, in the most general setting, a diffusion tensor depending on u. The left hand side of (3) is the Caputo fractional derivative defined by

$$\frac{{}^{C}\partial^{\alpha} u}{\partial t^{\alpha}} = \frac{1}{\Gamma(m+1-\alpha)} \int_0^t \frac{u^{(m+1)}(\tau)}{(t-\tau)^{\alpha-m}} d\tau\,,$$

with $m = \lfloor \alpha \rfloor$ (see [37]), where $0 < \alpha < 1$ (modelling sub-diffusion) or $1 < \alpha < 2$ (modelling super-diffusion). Since we want to apply this process to image processing, we restrict our attention to the two-dimensional space and assume further that κ is a given constant. Hence, a solution $u(\mathbf{x}, t)$ with $\mathbf{x} = (x, y)$ for some $0 < t < T$ is sought. To make (3) solvable for sub-diffusion, we specify the initial condition $u(\mathbf{x}, 0) = u^{(0)}(\mathbf{x})$, where $u^{(0)}$ is a given gray-value image. If super-diffusion is supposed, a second initial condition $u^{(1)}(\mathbf{x}) = \frac{\partial}{\partial t} u(\mathbf{x}, t)|_{t=0}$ has to be specified. Additionally, homogeneous Neumann boundary conditions are imposed for both sub- and super-diffusion. Since (3) cannot be solved analytically, it is discretised in space and in time.

The discretisation in space is straightforward using a two-dimensional grid with grid size $h = 1$ in both directions; i.e. the number of grid points is $M \times N$ (the given

resolution of the image $u^{(0)}$), the discretisation of the right hand side of (3) for interior nodes is given by (see also [7, p. 691])

$$\kappa \left(u_{i+1,j} + u_{i-1,j} + u_{i,j+1} + u_{i,j-1} - 4u_{i,j} \right) ,$$

since we used centred differences as follows

$$\left.\frac{\partial^2 u}{\partial x^2}\right|_{\mathbf{x}=(x_i,y_j)} \approx u_{i+1,j} - 2u_{i,j} + u_{i-1,j} \qquad \left.\frac{\partial^2 u}{\partial y^2}\right|_{\mathbf{x}=(x_i,y_j)} \approx u_{i+1,j} - 2u_{i,j} + u_{i-1,j} .$$

The discretisation for the boundary points looks slightly different due to the given homogeneous Neumann boundary conditions (as discussed later). More elaborate is the discretisation in time for the left hand side of (3). For a given $P \in \mathbb{N}$, we use a equidistant grid of the form $t_k = k \cdot \Delta t$, $k = 0, \ldots, P$ with grid size $\Delta t = T/P$. The Caputo fractional derivative of order α is approximated by

$$\left.\frac{{}^C\partial^\alpha u}{\partial t^\alpha}\right|_{\mathbf{x}=(x_i,y_j)}^{t=t_{k+1}} \approx \sum_{\ell=0}^{k+1} c_\ell^{(\alpha)} u_{i,j}^{k+1-\ell} - \sum_{n=0}^{m} \frac{(t_{k+1})^{n-\alpha}}{\Gamma(n-\alpha+1)} u^{(n)}(x_i, y_j) , \tag{4}$$

where $m = \lfloor \alpha \rfloor$, the $c_\ell^{(\alpha)}$ define the Grünwald-Letnikov coefficients and $u^{(n)}(x_i, y_j)$ are the initial conditions (see also [10, 37]). The Grünwald-Letnikov coefficients can be computed recursively by

$$c_0^{(\alpha)} = (\Delta t)^{-\alpha} , \qquad c_k^{(\alpha)} = \left(1 - \frac{1+\alpha}{k}\right) c_{k-1}^{(\alpha)}$$

with $k \in \mathbb{N}$ (see for example [37, p. 48]). In sum, the explicit time discretisation (see for example [7, p. 701]) of the fractional diffusion equation is given by

$$\begin{aligned} & \sum_{\ell=0}^{k+1} c_\ell^{(\alpha)} u_{i,j}^{k+1-\ell} - \sum_{n=0}^{m} \frac{(t_{k+1})^{n-\alpha}}{\Gamma(n-\alpha+1)} u^{(n)}(x_i, y_j) \\ = \;& \kappa \left(u_{i+1,j}^k + u_{i-1,j}^k + u_{i,j+1}^k + u_{i,j-1}^k - 4u_{i,j}^k \right) \end{aligned}$$

and the implicit discretisation (see for example [7, p. 703]) is given by

$$\begin{aligned} & \sum_{\ell=0}^{k+1} c_\ell^{(\alpha)} u_{i,j}^{k+1-\ell} - \sum_{n=0}^{m} \frac{(t_{k+1})^{n-\alpha}}{\Gamma(n-\alpha+1)} u^{(n)}(x_i, y_j) \\ = \;& \kappa \left(u_{i+1,j}^{k+1} + u_{i-1,j}^{k+1} + u_{i,j+1}^{k+1} + u_{i,j-1}^{k+1} - 4u_{i,j}^{k+1} \right) , \end{aligned}$$

respectively. The straightforward approach to obtain an easy to implement numerical

scheme is to rearrange the previous two equations to

$$u_{i,j}^{k+1} = (\Delta t)^{\alpha} \left(\kappa \left(u_{i+1,j}^{k} + u_{i-1,j}^{k} + u_{i,j+1}^{k} + u_{i,j-1}^{k} - (4 - \frac{\alpha(\Delta t)^{-\alpha}}{\kappa}) u_{i,j}^{k} \right) - \sum_{\ell=2}^{k+1} c_{\ell}^{(\alpha)} u_{i,j}^{k+1-\ell} + \sum_{n=0}^{m} \frac{(t_{k+1})^{n-\alpha}}{\Gamma(n-\alpha+1)} u^{(n)}(x_i, y_j) \right)$$

and

$$\begin{aligned} &- \alpha(\Delta t)^{-\alpha} u_{i,j}^{k} + \sum_{\ell=2}^{k+1} c_{\ell}^{(\alpha)} u_{i,j}^{k+1-\ell} - \sum_{n=0}^{m} \frac{(t_{k+1})^{n-\alpha}}{\Gamma(n-\alpha+1)} u^{(n)}(x_i, y_j) \\ &= \kappa \left(u_{i+1,j}^{k+1} + u_{i-1,j}^{k+1} + u_{i,j+1}^{k+1} + u_{i,j-1}^{k+1} - (4 + \frac{(\Delta t)^{-\alpha}}{\kappa}) u_{i,j}^{k+1} \right), \end{aligned}$$

respectively. Using a lexicographic ordering for $u_{i,j}^{k}$ and $u_{i,j}^{k+1}$ and putting them into the vectors $\mathbf{u}^k$ and $\mathbf{u}^{k+1}$ of size $M \cdot N$ yields the following explicit and implicit iteration scheme written abstractly as

$$\mathbf{u}^{k+1} = A\,\mathbf{u}^{k} - \mathbf{b}_{ex}\,, \qquad k = 0, \ldots, P-1$$

with $A = \alpha I_{MN} + (\Delta t)^{\alpha} \kappa \cdot D_2$ and

$$B\,\mathbf{u}^{k+1} = \mathbf{b}_{im}\,, \qquad k = 0, \ldots, P-1$$

with $B = -(\Delta t)^{-\alpha} I_{MN} + \kappa \cdot D_2$. I_{MN} denotes the identity matrix of size $M \cdot N \times M \cdot N$ and D_2 is the discrete 2D-Laplacian including the Neumann boundary conditions given by (see [42])

$$D_2 = D_1^M \otimes I_N + I_M \otimes D_1^N$$

with the tridiagonal matrix D_1^K of size $K \times K$ given by

$$D_1^K = \begin{pmatrix} -1 & 1 & & & & & \\ 1 & -2 & 1 & & & & \\ & 1 & \ddots & \ddots & & & \\ & & \ddots & \ddots & & & \\ & & & & 1 & -2 & 1 \\ & & & & & 1 & -1 \end{pmatrix}.$$

Here, the operation $\otimes$ denotes the Kronecker product (see [22]). The vectors $\mathbf{b}_{ex}$ and $\mathbf{b}_{im}$ are given by

$$\mathbf{b}_{ex} = (\Delta t)^{\alpha} \left(\sum_{\ell=2}^{k+1} c_{\ell}^{(\alpha)} \mathbf{u}^{k+1-\ell} - \sum_{n=0}^{m} \frac{(t_{k+1})^{n-\alpha}}{\Gamma(n-\alpha+1)} \mathbf{u}^{(n)}(x_i, y_j) \right),$$

and

$$\mathbf{b}_{im} = -\alpha(\Delta t)^{-\alpha}\mathbf{u}^k + \left(\sum_{\ell=2}^{k+1} c_\ell^{(\alpha)}\mathbf{u}^{k+1-\ell} - \sum_{n=0}^{m}\frac{(t_{k+1})^{n-\alpha}}{\Gamma(n-\alpha+1)}\mathbf{u}^{(n)}(x_i,y_j)\right).$$

3. Dilation and erosion from continuous scale morphology

The equations

$$\frac{{}^C\partial^\alpha u}{\partial t^\alpha} = \pm\sqrt{\left(\frac{\partial u}{\partial x}\right)^2 + \left(\frac{\partial u}{\partial y}\right)^2} \tag{5}$$

describe the process of modified dilation and erosion, respectively. Again a given image $u^{(0)}$ is used as initial condition and homogeneous boundary conditions are prescribed. For $1 < \alpha < 2$ we have to specify a second initial condition $u^{(1)}$. The approximation of the Caputo fractional derivative is used for discretisation in time (see (4)) and in space the first-order finite difference method by Rouy-Tourin [38] is used with $h = 1$ in both directions.

Note that the method of our choice to solve the morphological transport equations is the Rouy-Tourin scheme (RT) [38] mainly due to its simplicity and stability. As a first order numerical scheme it displays results very similar to the Osher-Sethian scheme (OS-I) [33, 34]. Only slightly better, but more elaborate, is the second order variant of Osher-Sethian scheme (OS-II) [33, 40]. The flux-corrected-transport scheme (FCT) of Breuss and Weickert [5], however, performs very well with only a small amount of numerical dissipation. FCT utilises a standard scheme, RT, OS-I or OS-II, as an initial step, whose dissipative effects are then minimized in a second, rather elaborate corrector step.

Precisely, we obtain

$$\left.\frac{\partial u}{\partial x}\right|_{\mathbf{x}=(x_i,y_j)} \approx \max\left(-u_{i,j} + u_{i-1,j}, u_{i+1,j} - u_{i,j}, 0\right)$$

and

$$\left.\frac{\partial u}{\partial y}\right|_{\mathbf{x}=(x_i,y_j)} \approx \max\left(-u_{i,j} + u_{i,j-1}, u_{i,j+1} - u_{i,j}, 0\right).$$

Accordingly, the spatial discretisation of the right hand side of (5) is given by

$$\left\{\max\left(-u_{i,j} + u_{i-1,j}, u_{i+1,j} - u_{i,j}, 0\right)^2 + \max\left(-u_{i,j} + u_{i,j-1}, u_{i,j+1} - u_{i,j}, 0\right)^2\right\}^{1/2}$$

and altogether after choosing the time t_k for the right hand side and rearranging terms

yields the following explicit method for (5)

$$\begin{aligned} u_{i,j}^{k+1} =& \alpha u_{i,j}^{k} - (\Delta t)^{\alpha} \sum_{\ell=2}^{k+1} c_{\ell}^{(\alpha)} u_{i,j}^{k+1-\ell} + (\Delta t)^{\alpha} \sum_{n=0}^{m} \frac{(t_{k+1})^{n-\alpha}}{\Gamma(n-\alpha+1)} u^{(n)}(x_i, y_j) \\ & \pm (\Delta t)^{\alpha} \Big\{ \max\Big(-u_{i,j}^{k} + u_{i-1,j}^{k}, u_{i+1,j}^{k} - u_{i,j}^{k}, 0\Big)^2 \\ & + \max\Big(-u_{i,j}^{k} + u_{i,j-1}^{k}, u_{i,j+1}^{k} - u_{i,j}^{k}, 0\Big)^2 \Big\}^{1/2} \end{aligned}$$

As before, we obtain an iterative scheme of the form

$$\mathbf{u}^{k+1} = \alpha \mathbf{u}^{k} + (\Delta t)^{\alpha} \mathbf{b}_{dt} \pm (\Delta t)^{\alpha} \sqrt{\mathbf{b}_{dx}^2 + \mathbf{b}_{dy}^2}\,, \qquad k = 0, \ldots, P-1\,,$$

where

$$\mathbf{b}_{dt} = -\sum_{l=2}^{k+1} c_{l}^{(\alpha)} \mathbf{u}^{k+1-l} + \sum_{n=0}^{m} \frac{(t_{k+1})^{n-\alpha}}{\Gamma(n-\alpha+1)} \mathbf{u}^{(n)}(x_i, y_j)$$

and the entries of $\mathbf{b}_{dx}$ are given by

$$\max\Big(-u_{i,j}^{k} + u_{i-1,j}^{k}, u_{i+1,j}^{k} - u_{i,j}^{k}, 0\Big)$$

and analogously $\mathbf{b}_{dy}$, where we have taken the homogeneous Neumann boundary conditions into account by mirroring the boundary values.

4. Numerical results

In this section, various numerical results are presented. First, we illustrate the stability regions for the explicit and implicit Euler method for different parameters of α. Then, it is shown that we are able to obtain first order accuracy using homogeneous initial conditions. In contrast to that the convergence rate depends on the parameter α for inhomogeneous initial conditions. The next subsection is devoted to numerical results for anomalous sub-diffusion followed by results for modified dilation, erosion, opening, and closing for $0 < \alpha \leq 1$. Additionally, a comparison of the results of the previous two subsections with the case of $\alpha = 1$ is provided. Finally, results for super-diffusion and modified dilation, erosion, opening, and closing for $1 < \alpha < 2$ are given. All numerical results are obtained by using Matlab R2015a.

4.1. *Stability*

It is well-known that the stability regions with respect to λ for the explicit and implicit Euler method applied to the linear test problem

$$\frac{{}^{C}\partial^{\alpha} u(t)}{\partial t^{\alpha}} = \lambda u(t)\,, \quad u(0) = u_0\,, \quad \lambda \in \mathbb{C}\,, \quad 0 < \alpha \leq 1 \tag{6}$$

and an additional initial condition of the form $u'(0) = u_1$ for $1 < \alpha < 2$ are given by

$$\mathbb{C}\setminus\{(1-z)^\alpha/z : |z| \le 1\} \text{ and } \mathbb{C}\setminus\{(1-z)^\alpha : |z| \le 1\}$$

(see for example [15, p. 571 & 572], [17, Figs. 2 & 3] and [29, 30] for the original work). In Figs. 1 and 2 we show the region of stability with color gray for the explicit and implicit Euler method for the parameters $\alpha = 0.4, 0.6, 0.8, 1.0, 1.2, 1.4$, respectively (compare also with [15, Fig. 1], [16, Fig. 1], and [17, Figs. 2 & 3]).

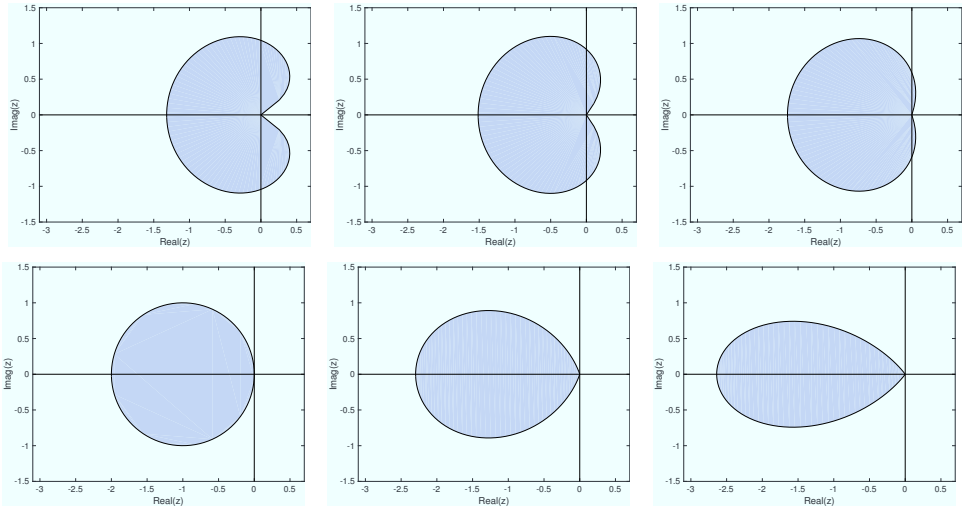

Figure 1. Stability regions for the explicit Euler method using the parameters $\alpha = 0.4$, $\alpha = 0.6$, and $\alpha = 0.8$ (first row) and $\alpha = 1.0$, $\alpha = 1.2$, and $\alpha = 1.4$ (second row).

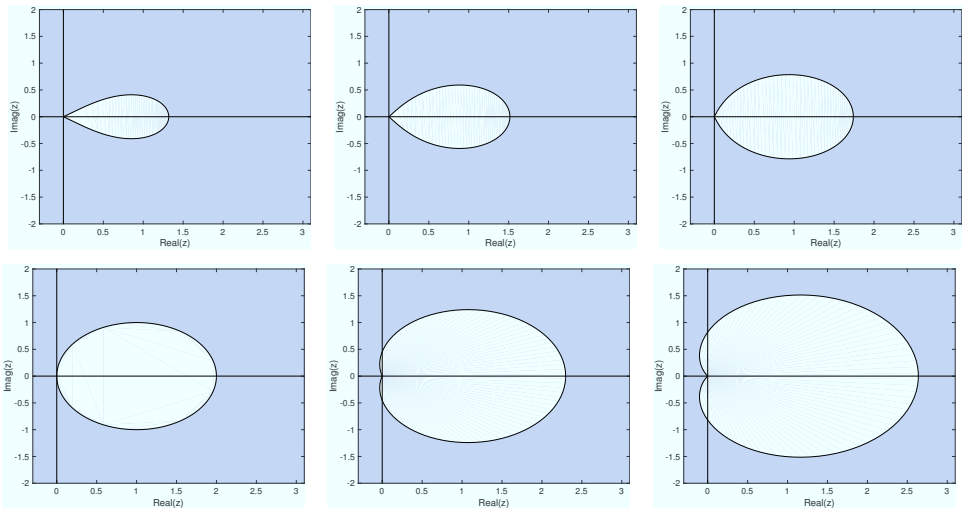

Figure 2. Stability regions for the implicit Euler method using the parameters $\alpha = 0.4$, $\alpha = 0.6$, and $\alpha = 0.8$ (first row) and $\alpha = 1.0$, $\alpha = 1.2$, and $\alpha = 1.4$ (second row).

Several conclusions can be drawn from these two figures. First, it is easy to see that the interval of stability for real λ for the explicit Euler method is smaller for $0 < \alpha < 1$ and larger for $1 < \alpha < 2$ compared to the case $\alpha = 1$. The interval of stability is given by $(-2^\alpha, 0)$. Second, the implicit Euler method is A-stable (see [19, Def. 2.1 on p. 268] for the definition) for $0 < \alpha \le 1$ whereas we loose this property for $1 < \alpha < 2$. Of

course, one could now investigate $A(\theta)$ stability (see [19, Def. 1.4 on p. 264] for the definition), where $\theta \leq \pi/2$ will depend on the parameter α. The next finding is both interesting and surprising, since we obtain integer values for the θ values. Precisely, we get the θ angles (in degrees $^\circ$) 90, 81, 72, 63, 54, 45, 36, 27, 18, and 9 for the parameters $\alpha = 1.0, 1.1, 1.2, 1.3, 1.4, 1.5, 1.6, 1.7, 1.8$, and 1.9, respectively. Hence, it appears to be that θ is given by $(2-\alpha)\cdot 90^\circ$ for $1 \leq \alpha < 2$ (the proof remains open).

4.2. *Convergence order*

It is also known that the discretization of the Caputo derivative as done above is first-order accurate both for the explicit and implicit Euler method independent of the parameter α provided that the initial condition is homogeneous (see [47, p. 109]). We can easily show this numerically by solving the fractional differential equation

$$\frac{{}^C\partial^\alpha u(t)}{\partial t^\alpha} = t^2\,, \quad u(0) = 0\,, \quad 0 \leq t \leq 1, \quad 0 < \alpha \leq 1$$

with exact solution

$$u(t) = \frac{\Gamma(3+\alpha)}{\Gamma(3)} t^{2+\alpha}\,.$$

which is constructed by calculating the Caputo fractional derivative of the power function $t^{2+\alpha}$. Note that for $1 < \alpha < 2$ we can use the same test since the second initial condition $u'(0) = 0$ is satisfied as well. In Table 1 we show the absolute error $E_{\Delta t} = |u(1) - \tilde{u}_{\Delta t}(1)|$, where $\tilde{u}_{\Delta t}(1)$ denotes the approximation of u at time $t = 1$, and the estimated order of convergence (EOC), which is given by

$$\text{EOC} = \log(E_{\Delta t}/E_{\Delta t/2})/\log(2)\,,$$

for the parameter $\alpha = 0.4, 0.8, 1.0$, and 1.2 using the explicit Euler method.

	$\alpha = 0.4$		$\alpha = 0.8$		$\alpha = 1.0$		$\alpha = 1.2$	
Δt	$E_{\Delta t}$	EOC	$E_{\Delta t}$	EOC	$E_{\Delta t}$	EOC	$E_{\Delta t}$	EOC
1/10	0.1220		0.0685		0.0483		0.0324	
1/20	0.0627	0.96	0.0350	0.97	0.0246	0.98	0.0164	0.99
1/40	0.0318	0.98	0.0177	0.98	0.0124	0.99	0.0082	1.00
1/80	0.0160	0.99	0.0089	0.99	0.0062	0.99	0.0041	1.00
1/160	0.0080	1.00	0.0045	1.00	0.0031	1.00	0.0021	1.00
1/320	0.0040	1.00	0.0022	1.00	0.0016	1.00	0.0010	1.00
1/640	0.0020	1.00	0.0011	1.00	0.0008	1.00	0.0005	1.00

Table 1. Estimated order of convergence for the explicit Euler method using the parameters $\alpha = 0.4, 0.8, 1.0$, and 1.2.

As we can observe in Table 1, we obtain first order accuracy for the explicit Euler method. The same holds true for the implicit Euler method as shown in Table 2, where we use the same parameters and initial conditions as before.

Furthermore, the errors are slightly better for the implicit Euler method for $0 < \alpha \leq 1$. The estimated order of convergence is linear and also slightly better for the implicit Euler method.

	$\alpha = 0.4$		$\alpha = 0.8$		$\alpha = 1.0$		$\alpha = 1.2$	
Δt	$E_{\Delta t}$	EOC	$E_{\Delta t}$	EOC	$E_{\Delta t}$	EOC	$E_{\Delta t}$	EOC
1/10	0.0323		0.0487		0.0517		0.0519	
1/20	0.0161	1.00	0.0241	1.01	0.0254	1.02	0.0253	1.03
1/40	0.0081	1.00	0.0120	1.01	0.0126	1.01	0.0125	1.02
1/80	0.0040	1.00	0.0060	1.00	0.0063	1.00	0.0062	1.01
1/160	0.0020	1.00	0.0030	1.00	0.0031	1.00	0.0031	1.00
1/320	0.0010	1.00	0.0015	1.00	0.0016	1.00	0.0015	1.00
1/640	0.0005	1.00	0.0007	1.00	0.0008	1.00	0.0008	1.00

Table 2. Estimated order of convergence for the implicit Euler method using the parameters $\alpha = 0.4, 0.8, 1.0,$ and 1.2.

It should be noted that in general we do not have first order convergence for the explicit and implicit Euler method provided non-homogeneous initial conditions are given. Then, the order of convergence will depend on the parameter α (see the discussion on page 109 in [47]). Interestingly, we encounter the same phenomenon if we use the simple fractional differential equation (6) with exact solution $u(t) = \mathrm{E}_\alpha(\lambda t^\alpha)u_0$. Here, $\mathrm{E}_\alpha(z)$ denotes the Mittag-Leffler function with $0 < \alpha < 1$ and $z \in \mathbb{C}$ (see for example [14, Section 18.1]). Using for example $u_0 = 1$, $\alpha = 1/2$ and $\lambda = -0.3$ with the same Δt's as used in Tables 1 and 2, we obtain the estimated order of convergence 0.48, 0.50, 0.50, 0.51, 0.51, 0.50 for the explicit and 0.57, 0.56, 0.55, 0.54, 0.53, 0.52 for the implicit Euler method, respectively. This clearly shows the dependence on α for the convergence rate. Of course, for a linear ODE it is always possible to use a transformation to obtain homogeneous initial conditions and then use the first order accurate solver. For the previous example, we can use the exact solution $v(t) = \mathrm{E}_\alpha(\lambda t^\alpha) - 1$ which satisfies

$$\frac{{}^C\partial^\alpha v(t)}{\partial t^\alpha} = \lambda(v(t) + 1)\,, \quad v(0) = 0\,, \quad \lambda \in \mathbb{C}\,, \quad 0 < \alpha \leq 1\,,$$

where we used the fact that the Caputo fractional derivative of order α of a constant is zero. Now, using $\alpha = 1/2$ and $\lambda = -0.3$ we are able obtain the estimated order of convergence 1.07, 1.04, 1.02, 1.01, 1.00, 1.00 for the explicit and 1.00, 1.00, 1.00, 1.00, 1.00, 1.00 for the implicit Euler method, respectively. This clearly indicates the linear order of convergence. Other parameter choices yield similar results as well. This is also the case if we use $1 < \alpha < 2$ with the second inital condition $v'(0) = 0$.

4.3. *Anomalous sub-diffusion*

Next, we present numerical results for (3) with homogeneous Neumann boundary conditions and the gray-value image Lena of size 512×512 as initial condition. The original Lena image is shown in Fig. 3 which is a well-known state-of-the-art test image that is widely used in the image processing community.

Using $\kappa = 1$, $h = 1$, and $\Delta t = 1/200$ for the implicit fractional diffusion scheme, $T = 1, 5, 10, 20$, and $\alpha = 1/2, 3/4, 1$ gives us the following results as shown in Fig. 4.

Using the fractional time derivative involves an integration in time which means an averaging, that is, smoothing in time. Visually, this fractional time-induced smoothing can hardly be distinguished from the spatial smoothing. This does not come as a surprise since the fractional time-induced smoothing is an averaging of grey values which have been the results of spatial averaging themselves. So in the end, one can

Figure 3. The Lena test image.

argue that everything boils down to a spatial averaging of intensities of the initial image. This is true, as can be seen from the effects on the presented images. However, this overall averaging process is quite involved, and fractional differentiation provides a splitting of this general smoothing into averaging in time and averaging in space (usually short distance, depending on the mask used in the numerical scheme). As a consequence the fraction α of the time derivative acts as a fine-tuning parameter in the general smoothing induced by the diffusion. This can be seen in Fig. 4 when comparing for example the two images generated with $T = 10$ and $\alpha = 1/2$ and $T = 5$ and $\alpha = 1$.

As it is well-known, linear diffusion ($\alpha = 1$) preserves the mean-value of an image. The Lena image has mean of approximately 124.1 and we obtain the same mean for $T = 10$ and $T = 20$ using $\alpha = 1$ (provided that Δt is small enough). The same is true for sub-diffusion.

4.4. *Modified dilation, erosion, opening, and closing for* $0 < \alpha \leq 1$

Next, we focus on the modified dilation process. Using $h = 1$ and $\Delta t = 1/200$ for the fractional dilation scheme, $T = 1, 5, 10, 20$, and $\alpha = 1/2, 3/4, 1$ gives us the following results as shown in Fig. 5.

Besides encountering the usual effects of continuous gray-value dilation with respect to the Euclidean norm (corresponding to a circular structuring element in set-valued morphology), one gets the impression that a very slight additional blurring occurs. This additional blurring is caused by the dissipative effects of the Rouy-Tourin numerical scheme. However, as expected, the fractional derivative slows down the evolution process the smaller α is. For the sake of completeness, we also show modified erosion for $T = 20$ using $\alpha = 1/2, 3/4, 1$ in Fig. 6.

Additionally, we show results for opening and closing in Fig 7 using the same parameters as before. The opening operation applied to an image consists of an erosion followed by a dilation with identical evolution times. Likewise, a dilation concatenated with an erosion yields the closing of an image. Since dilation and erosion are antagonistic processes, one can view both closing and opening as imperfect approximations to the identity operation. And it is this imperfection that is responsible for their image filtering powers.

We note in Fig. 7 that due to the antagonistic nature of dilation and erosion we can regard closing and opening as approximations to the identity operation. Clearly this approximation becomes more inaccurate the larger the evolution time is. For example, in the case of closing, the more the erosion of an image progresses, the more image details vanish, a loss that cannot be undone by a dilation. The same holds true for

(a) $T = 1$, $\alpha = 1/2$ (b) $T = 1$, $\alpha = 3/4$ (c) $T = 1$, $\alpha = 1$

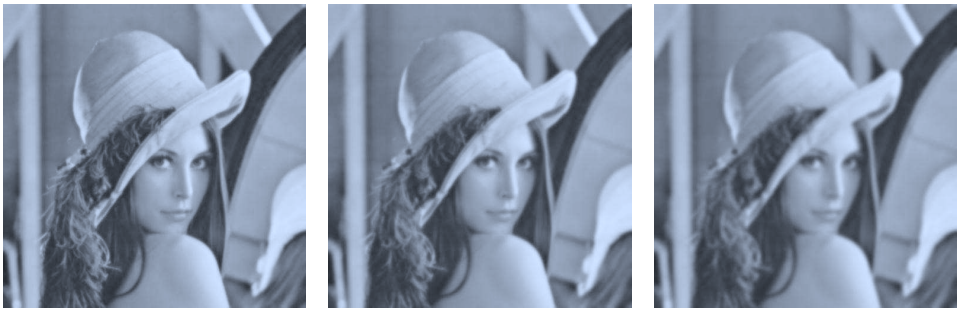

(d) $T = 5$, $\alpha = 1/2$ (e) $T = 5$, $\alpha = 3/4$ (f) $T = 5$, $\alpha = 1$

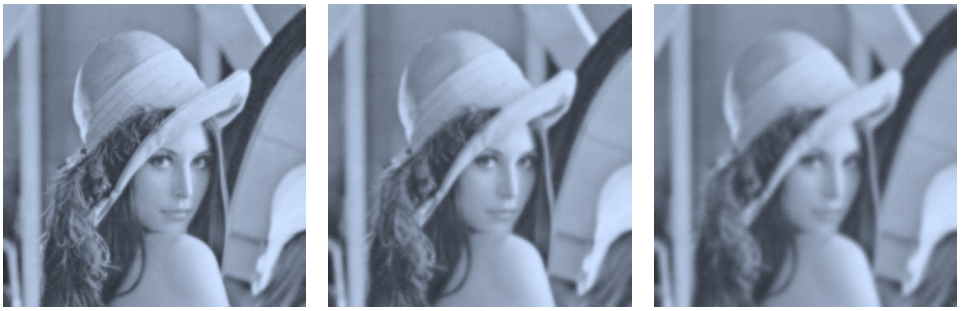

(g) $T = 10$, $\alpha = 1/2$ (h) $T = 10$, $\alpha = 3/4$ (i) $T = 10$, $\alpha = 1$

(j) $T = 20$, $\alpha = 1/2$ (k) $T = 20$, $\alpha = 3/4$ (l) $T = 20$, $\alpha = 1$

Figure 4. Anomalous sub-diffusion with the parameters $T = 1, 5, 10, 20$ and $\alpha = 1/2, 3/4, 1$ for the Lena image.

the process of opening. The results depicted in Figure 7 are in accordance with this reasoning: only large image structures (dark ones for closing, bright ones for opening) are preserved, while details are eliminated. Again the moderating effect of the α-value becomes apparent.

(a) $T = 1$, $\alpha = 1/2$ (b) $T = 1$, $\alpha = 3/4$ (c) $T = 1$, $\alpha = 1$

(d) $T = 5$, $\alpha = 1/2$ (e) $T = 5$, $\alpha = 3/4$ (f) $T = 5$, $\alpha = 1$

(g) $T = 10$, $\alpha = 1/2$ (h) $T = 10$, $\alpha = 3/4$ (i) $T = 10$, $\alpha = 1$

(j) $T = 20$, $\alpha = 1/2$ (k) $T = 20$, $\alpha = 3/4$ (l) $T = 20$, $\alpha = 1$

Figure 5. Modified dilation with the parameters $T = 1, 5, 10, 20$ and $\alpha = 1/2, 3/4, 1$ for the Lena image.

4.5. *Comparison to the case* $\alpha = 1$

At first, it seems reasonable to consider a scaled difference of two images to show the effect for varying parameter α. However, in order to make the difference more tangible, we employ a finer measure to compare results, the so called co-histogram. The co-histogram of two images $f(x, y)$ and $g(x, y)$ of resolution $M \times N$ is given by

(a) $T = 20$, $\alpha = 1/2$ (b) $T = 20$, $\alpha = 3/4$ (c) $T = 20$, $\alpha = 1$

Figure 6. Modified erosion with the parameters $T = 20$ and $\alpha = 1/2, 3/4, 1$ for the Lena image.

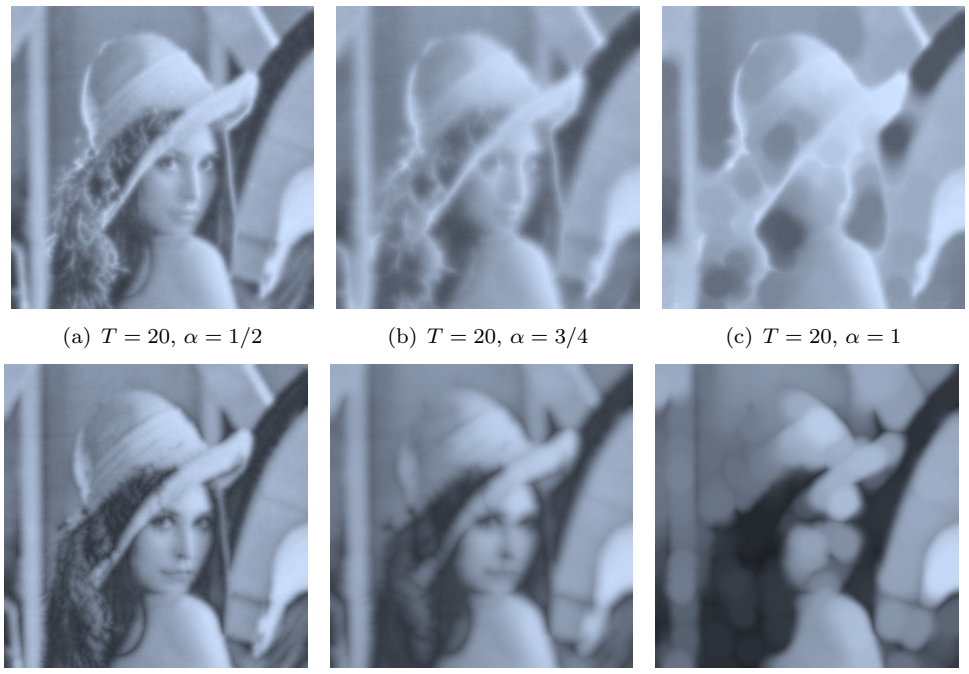

(a) $T = 20$, $\alpha = 1/2$ (b) $T = 20$, $\alpha = 3/4$ (c) $T = 20$, $\alpha = 1$

(d) $T = 20$, $\alpha = 1/2$ (e) $T = 20$, $\alpha = 3/4$ (f) $T = 20$, $\alpha = 1$

Figure 7. Modified opening (first row) and modified closing (second row) with the parameters $T = 20$ and $\alpha = 1/2, 3/4, 1$ for the Lena image.

all pixel value pairs (p, q), $H(p, q)$, where $H(p, q)$ is given by

$$H(p,q) = \frac{1}{MN} \sum_{y=1}^{M} \sum_{x=1}^{N} \delta(f(x,y), p)\delta(g(x,y), q)\,,$$

where $\delta(f, p)$ denotes the Kronecker delta function (see [20] for more details). The value $H(p, q)$ represents the probability that the value of ordered image pair (f, g) coincides with the gray-value pair (p, q) anywhere in the whole image domain. Hence, a co-histogram comparing an image with itself is represented by a black 256×256-image except that its diagonal consists of white pixels (gray-value is one). However, for a better visualization we depict the inverted image $1 - H(p, q)$, see Figs. 8 and 9. Comparing identical images would lead to an inverted co-histogram which is white (gray-value is one) except a black (gray-value is zero) diagonal. Hence, the larger the

deviation from this "diagonality" is, the larger is the difference between the compared images. Note that this is a global measure and it is rather difficult to infer local information about the difference of images from their co-histogram due to the coding of the pixel pairs.

In Fig. 8, we show six co-histograms for various sub-diffusion with the regular diffusion (inverted for better visibility and scaled to the full gray-value range). The first row uses the parameter $\alpha = 1/2$ and the second row uses the parameter $\alpha = 3/4$. The first, second, and third column use the parameters $T = 5$, $T = 10$, and $T = 20$.

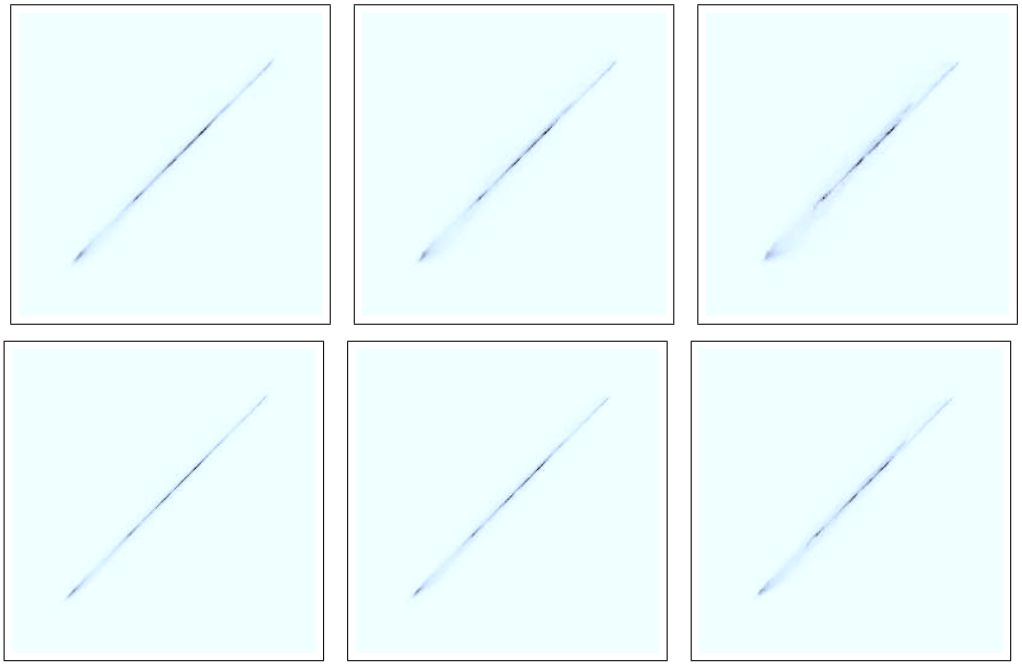

Figure 8. Inverted co-histograms for anomalous diffusion using the parameters $T = 5$, $T = 10$, and $T = 20$ (column) and $\alpha = 1/2$ and $\alpha = 3/4$ (row) compared to diffusion with $\alpha = 1$.

In case of anomalous diffusion we note a shortening of the diagonal in all of the depicted co-histogram comparisons. This is due to the fact that in natural images diffusion preferably eliminates very large and small gray-values, if they are present at all. Otherwise, we do not see a significant deviation from diagonality with a most prominent difference in the case of $\alpha = 1/2$ and $T = 20$. Next, we also show the co-histograms for the dilation process. We use the same parameters as before and obtain the following co-histograms as shown in Fig. 9.

In case of anomalous dilation a general shortening of the diagonal in all of the inverted histograms is even more pronounced, which can be understood by disproportionally large influence of dilation on pixels with extreme gray-values. In comparison with the case of diffusion the diagonal is more smeared out and the influence of the parameter α on the evolution process is larger, again with the most significant difference for the parameter values $\alpha = 1/2$ and $T = 20$.

However, we did not yet fully exploit the potential of the concept of co-histograms, especially its quantitative powers rather than its qualitative aspects. We will concentrate on this in future research which will focus on fractional variants of more involved evolution equations (accessible to level-set-methods) where the time dependence of the results is more sensitive than in the case of a simple linear diffusion. We expect a greater impact of the use of the fractional time derivative on the outcome of the

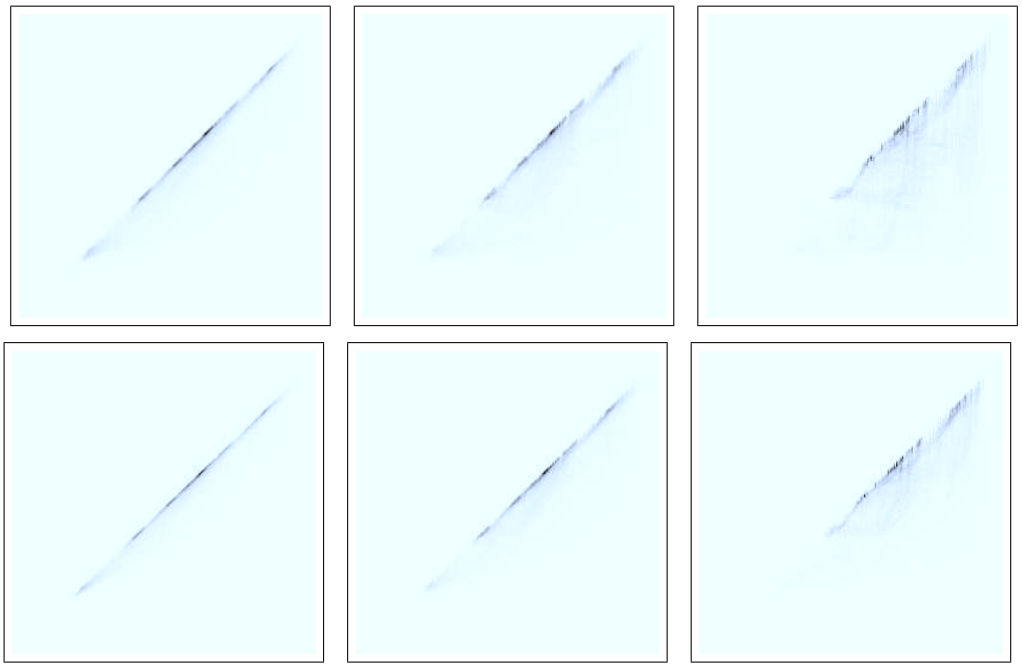

Figure 9. Inverted co-histograms for modified dilation using the parameters $T = 5$, $T = 10$, and $T = 20$ (column) and $\alpha = 1/2$ and $\alpha = 3/4$ (row) compared to dilation with $\alpha = 1$.

evolution processes.

4.6. *Anomalous super-diffusion, modified dilation, erosion, opening, and closing for* $1 < \alpha < 2$

Finally, we show results for super-diffusion and the modified dilation/erosion using the same parameters as before. Note that we have several choices for the second initial condition. We could for example use a homogeneous initial condition or possibly the given image itself as the second initial condition. Instigated by the treatment in [50], we opt for a vanishing second initial condition since for $\alpha = 2$ (the case of a wave-equation), these would correspond to a zero-velocity initial field. Therefore, this seems to be a natural assumption. In Fig. 10 we show results for $\alpha = 1.1$ (first row) and $\alpha = 1.2$ (second row) for anomalous super-diffusion (first column), modified dilation (second column), and modified erosion (third) column using $T = 1$ and $T = 10$.

The first column in Fig. 10 depicts the results of diffusion using as second initial condition zero (this corresonds to a black image) as already mentioned before. In the case of anomalous diffusion, an increasing α-value (larger one) seems to have a slightly accelerating effect on the smoothing, if compared with the results of regular diffusion ($\alpha = 1$) as depicted in Fig. 4. One can also discern a mild brightening of the evolved image. Surprisingly, for the morphological operations the evolution depends sensitively on α (note the short evolution time $T = 1$) and leads to a much brighter image for dilation and a much darker image for erosion. This tendency is more pronounced the larger α is. At time $T = 1$ the actual dilation resp. erosion process of the underlying image has not shown clearly visible effects yet. It appears that the solutions to the modified transport equations given in (5) mimicking dilation and erosion react very sensitive to the presence of a second initial condition more than their counterparts in the case of sub-diffusion. In essence, the role played by this second initial condition is

(a) $T = 10$, $\alpha = 1.1$ (b) $T = 1$, $\alpha = 1.1$ (c) $T = 1$, $\alpha = 1.1$

(d) $T = 10$, $\alpha = 1.2$ (e) $T = 1$, $\alpha = 1.2$ (f) $T = 1$, $\alpha = 1.2$

Figure 10. Anomalous super-diffusion, modified dilation, and erosion for $\alpha = 1.1$ (first row) and $\alpha = 1.2$ (second row) with the parameter $T = 1$ and $T = 10$ for the Lena image.

not yet fully understood and hence is subject to future research.

5. Summary and outlook

On the one side, in this paper we modified standard gray-value diffusion of images by employing Caputo fractional derivatives of order $\alpha \in (0, 2)$ instead of the usual first order derivative in the time domain. The resulting anomalous sub- and super-diffusion process is treated numerically by means of explicit and implicit Euler methods. On the other side, we applied the same changes to the transport equations describing dilation and erosion, the building blocks of continuous scale morphology. We adapted the Rouy-Tourin-scheme to the Caputo fractional derivative setting to obtain our numerical results. Fine-tuned comparisons by means of co-histograms illustrate the potential as well as the shortcomings of this anomalous evolution process in the processing of gray-value images. With our approach we are capable to produce images with either sub-diffusion or super-diffusion which then might serve as testing examples for algorithm such as image deblurring which are theoretically based on linear diffusion.

In our future work, we will consider second-order approximations of the Caputo fractional derivative in order to improve the overall rate of convergence. In this context, it will also be worthwhile to investigate the usage of multistep methods (BDF, Adams-Moulton, and Adams-Bashforth methods), see [15] or the recent article [3]. The consideration of related inverse problems for anomalous diffusion is interesting in its own right (refer to [26]).

Additionally, it is now also possible to consider higher morphological operations such as opening, closing, and various morphological gradients. The investigation of fractional modifications of other highly nonlinear PDE-based image processing filters

seems to be promising, too. The extension of this new approach for color images or multispectral images would be a new research direction as well (see for example [4, 8, 27]).

Acknowledgement

The authors would like to thank the guest editors and the two anonymous referees for their valuable and detailed comments that led to a major improvement of the original manuscript.

References

[1] A. Atangana and A. Secer, *A note on fractional order derivatives and table of fractional derivatives of some special functions*, Abstract and Applied Analysis 2013 (2013), p. 279681.

[2] A. Atangana and A. Secer, *The time-fractional coupled-Korteweg-de-Vries equations*, Abstract and Applied Analysis 2013 (2013), p. 947986.

[3] D. Baffet and J.S. Hesthaven, *High-order accurate local schemes for fractional differential equations*, Journal of Scientific Computing 70 (2017), pp. 355–385.

[4] A.S. Boroujerdi, M. Breuß, B. Burgeth, and A. Kleefeld, *PDE-Based Color Morphology Using Matrix Fields*, in *Scale Space and Variational Methods in Computer Vision, 5th International Conference, SSVM 2015, Lège-Cap Ferret, France, May 31 – June 4, 2015, Proceedings*, J.F. Aujol, M. Nikolova, and N. Papadakis, eds. 2015, pp. 461–473.

[5] M. Breuß and J. Weickert, *A shock-capturing algorithm for the differential equations of dilation and erosion*, Journal of Mathematical Imaging and Vision 25 (2006), pp. 187–201.

[6] R.W. Brockett and P. Maragos, *Evolution equations for continuous-scale morphology*, in *Proc. IEEE International Conference on Acoustics, Speech and Signal Processing*, Vol. 3, San Francisco, CA. 1992, pp. 125–128.

[7] R.L. Burden and J.D. Faires, *Numerical Analysis*, Cengage Learning, 2005.

[8] B. Burgeth and A. Kleefeld, *An approach to color-morphology based on Einstein addition and Loewner order*, Pattern Recognition Letters 47 (2014), pp. 29–39.

[9] B. Burgeth, S. Didas, and J. Weickert, *The Bessel Scale-Space*, in *Deep Structure, Singularities, and Computer Vision: First International Workshop, DSSCV 2005, Maastricht, The Netherlands, June 9-10, 2005, Revised Selected Papers*, O. Fogh Olsen, L. Florack, and A. Kuijper, eds., Berlin. Springer, 2005, pp. 84–95.

[10] M. Caputo, *Linear models of dissipation whose q is almost frequency independent*, II. Geophys. J. Royal. Astronom. Soc. 13 (1967), pp. 529–539.

[11] E. Cuesta, M. Kirane, and S.A. Malik, *Image structure preserving denoising using generalized fractional time integrals*, Signal Processing 92 (2012), pp. 553–563.

[12] S. Das and I. Pan, *Fractional Order Signal Processing: Introductory Concepts and Applications*, SpringerBriefs in Applied Sciences and Technology, Springer, 2011.

[13] J. Davis, S.R. Marschner, M. Garr, and M. Levoy, *Filling holes in complex surfaces using volumetric diffusion*, in *Proceedings. First International Symposium on 3D Data Processing Visualization and Transmission.* 2002, pp. 428–441.

[14] A. Erdélyi, W. Magnus, F. Oberhettinger, and F.G. Tricomi, *Higher Transcendental Functions*, Vol. 3, McGraw-Hill, New York, 1955.

[15] L. Galeone and R. Garrappa, *On multistep methods for differential equations of fractional order*, Mediterranean Journal of Mathematics 3 (2006), pp. 565–580.

[16] L. Galeone and R. Garrappa, *Explicit methods for fractional differential equations and their stability properties*, Journal of Computational and Applied Mathematics 228 (2009), pp. 548–560.

[17] R. Garrappa, *Trapezoidal methods for fractional differential equations: Theoretical and computational aspects.*, Mathematics and Computers in Simulation 110 (2015), pp. 96–112.
[18] M.T. Gastner and M.E.J. Newman, *Diffusion-based method for producing density-equalizing maps*, Proceedings of the National Academy of Scinces of the United States of America 101 (2004), pp. 7499–7504.
[19] E. Hairer and G. Wanner, *Solving Ordinary Differential Equations II: Stiff and Differential-Algebraic Problems*, Springer Series in Computational Mathematics Vol. 14, Springer, 1991.
[20] P. Hao, C. Zhang, and A. Dang, *Co-histogram and image degradation evaluation*, in *Image Analysis and Recognition: International Conference ICIAR 2004, Porto, Portugal, September 29 - October 1, 2004, Proceedings, Part I*, A. Campilho and M. Kamel, eds., Berlin: Springer, 2004, pp. 195–203.
[21] R. Herrmann, *Fraktionale Infinitesimalrechnung*, Books on Demand GmbH, Norderstedt, 2008.
[22] R.A. Horn and C.R. Johnson, *Matrix Analysis*, Cambridge University Press, 1990.
[23] T. Iijima, *Basic theory of pattern observation*, in *Papers of Technical Group on Automata and Automatic Control*, IECE, Japan, 1959. (In Japanese).
[24] T. Iijima, *Basic equation of figure and observational transformation*, Systems, Computers & Controls 2 (1971), pp. 70–77.
[25] M. Janev, S. Pilipovic, T.M. Atanackovic, R. Obradovic, and N.M. Ralevic, *Fully fractional anisotropic diffusion for image denoising*, Mathematical and Computer Modelling 54 (2011), pp. 729–741.
[26] B. Jin and R. Rundell, *A tutorial on inverse problems for anomalous diffusion processes*, Inverse Problems 31 (2015), p. 035003.
[27] A. Kleefeld and B. Burgeth, *Processing multispectral images via mathematical morphology*, in *Visualization and Processing of Higher Order Descriptors for Multi-Valued Data*, I. Hotz and T. Schultz, eds., Springer, Berlin, 2015, pp. 129–148.
[28] J.J. Koenderink, *The structure of images*, Biological Cybernetics 50 (1984), pp. 363–370.
[29] C. Lubich, *Fractional linear multistep methods for Abel-Volterra integral equations of the second kind*, Mathematics of Computation 45 (1985), pp. 463–469.
[30] C. Lubich, *A stability analysis of convolution quadraturea for Abel-Volterra integral equations*, IMA Journal of Numerical Analysis 6 (1986), pp. 87–101.
[31] G. Matheron, *Eléments pour une théorie des milieux poreux*, Masson, Paris, 1967.
[32] K.B. Oldham and J. Spanier, *The Fractional Calculus*, Dover Publications, INC., Mineola, New York, 2006.
[33] S. Osher and R.P. Fedkiw, *Level Set Methods and Dynamic Implicit Surfaces*, Applied Mathematical Sciences Vol. 153, Springer, New York, 2002.
[34] S. Osher and J.A. Sethian, *Fronts propagating with curvature-dependent speed: Algorithms based on Hamilton–Jacobi formulations*, Journal of Computational Physics 79 (1988), pp. 12–49.
[35] P. Perona and J. Malik, *Scale-space and edge detection using anisotrophic diffusion*, IEEE Transactions on pattern analysis and machine intelligence 12 (1990), pp. 629–639.
[36] I. Petras, *Fractional derivatives, fractional integrals, and fractional differential equations in Matlab*, in *Engineering Education and Research Using MATLAB*. 2011, pp. 239–264.
[37] I. Podlubny, *Fractional Differential Equations: An Introduction to Fractional Derivatives, Fractional Differential Equations, to Methods of Their Solution and Some of Their Applications*, Vol. 198, Academic Press, 1998.
[38] E. Rouy and A. Tourin, *A viscosity solutions approach to shape-from-shading*, SIAM Journal on Numerical Analysis 29 (1992), pp. 867–884.
[39] J. Serra, *Echantillonnage et estimation des phénomènes de transition minier*, Ph.D. diss., University of Nancy, France, 1967.
[40] J.A. Sethian, *Level Set Methods and Fast Marching Methods*, 2nd ed., Cambridge University Press, Cambridge, UK, 1999, Paperback edition.

[41] P. Soille, *Morphological Image Analysis: Principles and Applications*, 2nd ed., Springer, New York, 2003.
[42] L.N. Trefethen, *Spectral Methods in MATLAB*, Software, Environments, and Tools, Society for Industrial and Applied Mathematics, 2000.
[43] R. van den Boomgaard, *Mathematical morphology: Extensions towards computer vision*, Ph.D. diss., University of Amsterdam, The Netherlands, 1992.
[44] R. van den Boomgaard, *Numerical solution schemes for continuous-scale morphology*, in *Scale-Space Theories in Computer Vision*, M. Nielsen, P. Johansen, O.F. Olsen, and J. Weickert, eds., LNCS Vol. 1682, Springer, Berlin, 1999, pp. 199–210.
[45] R. Wang and D. Tao, *Recent progress in image deblurring*, arXiv:1409.6838 (2014), pp. 1–57.
[46] J. Weickert, *Anisotropic diffusion in image processing*, ECMI series, Teubner, Stuttgart, 1998.
[47] M. Weilbeer, *Efficient numerical methods for fractional differential equations and their analytical background*, Ph.D. diss., Technische Universität Braunschweig, 2005.
[48] A.P. Witkin, *Scale-space filtering*, in *Proc. Eighth International Joint Conference on Artificial Intelligence*, Vol. 2, Karlsruhe, Germany. 1983, pp. 945–951.
[49] Q. Yang, D. Chen, T. Zhao, and Y.Q. Chen, *Fractional calculus in image processing: a review*, Fractional Calculus and Applied Analysis 19 (2016), pp. 1222–1249.
[50] W. Zhang, J. Li, and Y. Yang, *A fractional diffusion-wave equation with non-local regularization for image denoising*, Signal Processing 103 (2014), pp. 6–15.